Composites Science and Technology 242 (2023) 110197

Contents lists available at ScienceDirect

Composites Science and Technology

journal homepage: www.elsevier.com/locate/compscitech

Study on mechanical properties of polyurethane-enhanced triply periodic minimal composite structures inspired by rachis microstructure

Ruiyao Liu [a], Guofeng Yao [a], Luming Sha [b], Zhenglei Yu [b,c,*], Ping Liang [b,**], Chunyang Han [d], Keyi Zhu [e], Lei Dong [f], Zezhou Xu [b,****], Jundong Zhang [b], Yunting Guo [b,***]

[a] Department of Mechanics, School of Mechanical and Aerospace Engineering, Jilin University, Changchun, 130022, China
[b] Key Laboratory of Bionic Engineering of Ministry of Education, Jilin University, Changchun, 130022, China
[c] State Key Laboratory of Automotive Simulation and Control, Jilin University, Changchun, 130022, China
[d] Changchun Institute of Optics, Fine Mechanics and Physics, Chinese Academy of Sciences, Changchun, 130022, China
[e] Jilin Guoke Innovation Incubation Investment Co., Ltd, Changchun, 130000, China
[f] FAW Mould Manufacturing Co., Ltd, Changchun, 130000, China

ARTICLE INFO

Handling Editor: Prof. W. Yang

Keywords:
Bionic
Euler theory
Transfer path deviation
Triply periodic minimal composite structures
Energy dissipation

ABSTRACT

Inspired by the micro-curved structure and microfiber filling of the feather, four novel polyurethane-enhanced triply periodic minimal composite structures are designed. Based on Euler theory and simulated annealing algorithm, the mechanical relationships of enhanced composite structures at the compression and impact stage are deduced and predicted. The polyurethane-enhanced composite structure is larger than the corresponding triply periodic minimal structure in the average load. The specific energy absorption of the polyurethane-enhanced triply periodic minimal composite structure is at least 10% better than the original. Through the energy expansion of the foam, the energy transfer path is allowed to deviate in the foam. And the load distribution is not only in the vertical direction but also in the transverse direction. All these factors (more energy dissipation and transfer path deviation) work to improve the crashworthiness of polyurethane-enhanced composite structures. The impact videos are captured by high-speed photography FASTCAM Nova R2. The reduction of normalized stress is proved in the design of polyurethane-enhanced structure, and the reduction of the impact acceleration of polyurethane-enhanced composite structure is more than 13.6%. This bio-inspired rigid-flexible coupling design of composite structure is crucial to the novel design of the next generation.

1. Introduction

There are many ways to obtain inspiration for porous structures, such as topology optimization and bio-inspired optimization design [1–3]. These porous designs can be further optimized by structural embedding, cell size, and material selection [4–7]. Porous structures have been widely used in various engineering applications due to their excellent mechanical properties such as lightweight, high strength, high specific energy absorption, and strong strain rate efficiency [8–10]. Hybrid curved porous designs and reinforced material-filled composite structures have attracted the attention of researchers because they can improve the mechanical properties of porous structures by modifying their mechanical properties and controlling deformation modes through porosity, size, and other local modifications [11–15]. In nature, there are a variety of continuous porous structures with excellent mechanical properties inside the organism, such as the shell gradient layer [16], the porous structure of the femur [17], and the feather gradient porous structure [18]. Better design of porous structures with excellent properties is called a hot topic for researchers in various countries.

In recent years, researchers have turned their attention to a new type of porous metamaterial with the development and deepening research of metamaterials science. The novel type of porous design is the porous structure defined by mathematical functions, such as the porous structure composed of periodic triply periodic minimal structure (TPMS)

* Corresponding author. Key Laboratory of Bionic Engineering of Ministry of Education, Jilin University, Changchun, 130022, China.
** Corresponding author.
*** Corresponding author.
**** Corresponding author.
E-mail addresses: zlyu@jlu.edu.cn (Z. Yu), Liangping@jlu.edu.cn (P. Liang), ytguo@jlu.edu.cn (Y. Guo).

https://doi.org/10.1016/j.compscitech.2023.110197
Received 9 February 2023; Received in revised form 28 June 2023; Accepted 29 July 2023
Available online 4 August 2023

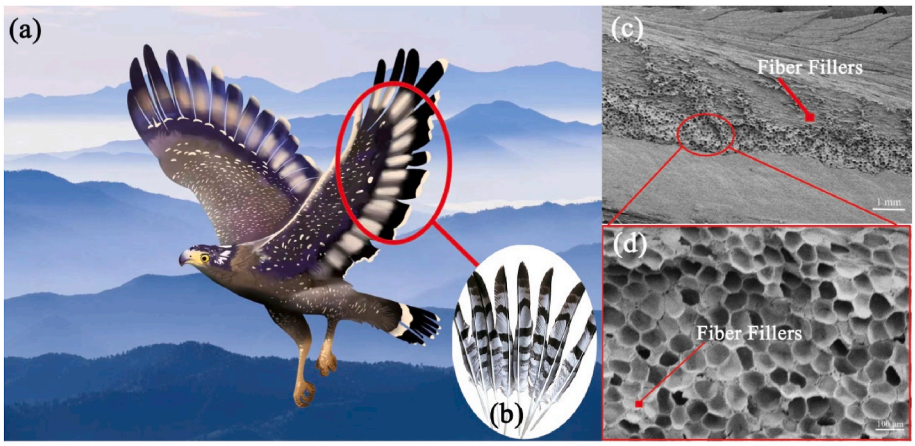

Fig. 1. The microscopic porous composition of the rachis microstructure; (a) Spilornis Cheela; (b) Spilornis Cheela feather; (c) 1 mm Electron microscopy of the rachis; (d) 100 μm Electron microscopy of rachis.

[19], and the porous Voronoi structure [20]. Among them, the porous structure composed of periodic triply periodic minimal structure (TPMS) is considered to be one of the most valuable porous structures [21]. It is of great research value to design multi-angle TPMS. Therefore, it is necessary to make full use of additive manufacturing (AM) technology to fabricate and test the mechanical properties of gradient porous structures with different scaffold sizes and morphologies [22–24]. In the ideal state, the bio-inspired structure designed by mathematical function definition is continuous and coherent in space, and the surface expansion area has uniform curvature [25]. The configuration of the transition surface makes the porous structure have a higher uniform stress distribution [26–28]. Based on the minimizing bending energy method, Bonatti et al. [29] designed a smooth structure with special energy absorption and studied the mechanical properties of the elastic isotropic derivatives of TPMS with the same density. Chen et al. [30] combined different surfaces in porous structures to change young's modulus and shear modulus. It is proved that the structural performance of the optimized surface design is better than other structures. Shen et al. [31] summarized the potential value of TPMS with excellent mechanical properties in lightweight structural design applications. Al-Ketan [32] studied the relationship between the size and the compressive mechanical properties of TPMS. Yin et al. [33] studied the dynamic crushing mechanical behavior of four TPMS at different speeds. Inspired by the self-intersecting surface of the bone microstructure with controllable mechanical properties, Tran et al. [34] studied the dynamic behavior of the novel TPMS composite plate under extreme load and obtained protective performance under explosive load.

From the perspective of manufacturing, the complex geometric characteristics of TPMS make its structural manufacturing extremely challenging [35,36]. Compared with traditional manufacturing methods, additive manufacturing has irreplaceable advantages and can effectively solve the difficulties and challenges encountered in the manufacturing of TPMS. For non-metallic AM, the most commonly used methods are fused deposition manufacturing (FDM), photosensitive resin selective curing (SLA), and selective laser sintering (SLS). SLS efficiently prepares various types of porous materials with extremely high manufacturing accuracy, extremely high material utilization, and extremely low production costs [37–39]. The mechanical properties of Nylon and PLA porous structures prepared by SLS have been extensively studied under different loading conditions [40–42]. Mishra et al. [43] compared the mechanical behavior of TPMS composed of two different polymers (PLA and ABS) and obtained stress and deformation performance under different printing materials and different uniaxial compression speeds. Based on the fused deposition modeling (FDM) technique, Monkova et al. [44] studied the effects of unit size and volume ratio of body-centered cubic lattice (BCC) on its mechanical vibration reduction and compression performance. Gautam et al. [45] focused on the influence of structural orientation, truss radius, and surface roughness of ABS Kagome truss structure prepared by FDM on compressive strength and stiffness. Based on different lattice structures of additive manufacturing, Al Rifaie et al. [46] studied the stiffness, failure load, and energy absorption behavior of lattice structures with different configurations. However, filled porous structures still face some challenges and issues in the manufacturing process [47]. The shape and size of filled porous structures limit their performance, which may restrict their application range. Similarly, the filling material plays a crucial role in the performance of filled porous structures [48]. At present, there are still problems such as uneven distribution of the filling material and insufficient adhesion between the filling material and the matrix, which directly affects the performance of porous structures [49]. Meanwhile, experimental data and computational studies of polyurethane-enhanced composite structures fabricated by additive manufacturing are very limited.

Considering the aforementioned problems, the design, manufacturing, and mechanical performance analysis of filled biomimetic composite structures have been conducted, providing effective research and application references for the analysis of filled porous structures. Inspired by the microscopic lattice structure of feathers, polyurethane-enhanced triply periodic minimal composite structures printed by SLS technology are studied. Based on Euler theory, mechanical relationships of enhanced composite structures at the compression and impact stage are deduced. The compression performance of triply periodic minimal structures and polyurethane-enhanced triply periodic minimal composite structures are studied by experiments and modeling methods. The load distribution and deformation mode of the structures are discussed. All these factors (more energy dissipation and transfer path deviation) work together to improve the crashworthiness of polyurethane-enhanced triply periodic minimal composite structures. To deepen the influence on the compression performance of rigid-flexible coupling composite structure, the structural elastic modulus is predicted based on Euler theorem and the simulated annealing algorithm, and the accuracy of the results is verified by experiments.

2. Structural design and manufacturing

2.1. Polyurethane-enhanced triply periodic minimal composite structure design

The inspiration for the polyurethane-enhanced composite structure comes from the microscopic porous composition of the rachis microstructure. Fig. 1 shows the scanning electron microscope (SEM) figure of

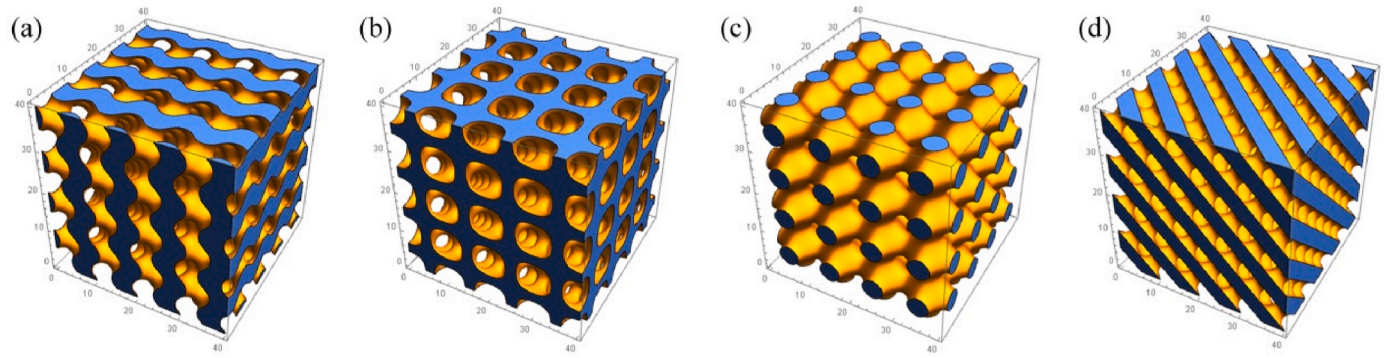

Fig. 2. Triply periodic minimal structure; (a) Gyroid structure, the formula as Eq. (1); (b) IWP structure, the formula as Eq. (2); (c) Primitive structure, the formula as Eq. (3); (d) Diamond structure, the formula as Eq. (4).

Table 1
Structural design parameters of the triply periodic minimal unit.

	a	b	c	D
Gyroid	0.2π	0.2π	0.2π	0
Primitive	0.2π	0.2π	0.2π	0
Diamond	0.2π	0.2π	0.2π	0
IWP	0.2π	0.2π	0.2π	0

Spilornis Cheela rachis. It can be seen that the microstructure of the rachis presents a continuous curved porous structure and presents a mixed cross configuration [49,50]. And there are fine fiber fillers inside the micropores to support the overall structure, as shown in Fig. 1(d).

The triply periodic minimal structure has a bio-inspired configuration, and the surface is smooth everywhere, thus effectively avoiding the stress concentration phenomenon in the traditional lattice structure. The triply periodic minimal configuration makes structural load distribution more uniform and the material utilization rate higher. Mathematically, triply periodic minimal structures can be defined and designed by parameterized approximation equations [52].

In this paper, four kinds of triply periodic minimal structures are obtained by implicit functions $\Phi_i(x,y,z) = D_i, (i = G,I,P,D)$, as shown in Fig. 2. In the implicit function, $D_i(i = G,I,P,D)$ can adjust the volume fraction of the triply periodic minimal porous structure.

$$\Phi_G = \sin ax \cos by + \sin by \cos cz + \sin cz \cos ax = D_G \tag{1}$$

$$\Phi_I = \cos(ax)\cos(by) + \cos(by)\cos(cz) + \cos(cz)\cos(ax) = D_I \tag{2}$$

$$\Phi_P = \cos(ax) + \cos(by) + \cos(cz) = D_P \tag{3}$$

$$\Phi_D = \sin(ax)\sin(by)\sin(cz) + \sin(ax)\cos(by)\cos(cz) + \cos(ax)\sin(by)\cos(cz) + \cos(ax)\cos(by)\sin(cz) = D_D \tag{4}$$

where a, b, c are the periods of the triply periodic minimal structure in x, y, z directions, $a = 2\pi\frac{n_a}{L_a}$, $b = 2\pi\frac{n_b}{L_b}$, $c = 2\pi\frac{n_c}{L_c}$. $n_i(i = a,b,c)$ is the number of the triply periodic minimal unit in different directions. $L_i(i = a,b,c)$ denotes the length of the triply periodic minimal structure in different directions.

The implicit function with a relative density of 50% is written by MATLAB. And the three-dimensional triply periodic minimal structure truncated by x, y, z end is generated. The triply periodic minimal structure generation code is shown in attachment 1. The size of a single unit in the triply periodic minimal structure is designed to be 10 × 10 × 10 mm. The number of units in x, y, and z directions is 4 × 4 × 4. The structural design parameters of the triply periodic minimal unit are shown in Table 1.

However, these continuous triply periodic minimal structures are prone to pinch fracture and have low compressive properties. Therefore, to improve the bearing toughness and pinching defects of the designed structure, the polyurethane-enhanced composite structure is designed in combination with the self-filling characteristics of the rachis microstructure.

The filler in the filled triply periodic minimal composite structure is prepared to utilize the filling foaming method using polydiphenylmethane diisocyanate and the polyether polyol as raw materials. Add 10 ml polyether polyol to the disposable plastic cup and add the same amount of polydiphenylmethane diisocyanate. The electric variable-speed stirrer ANgni with 1000 rpm digital display stirs the mixture for 10–15 s. The mixture is poured into a disposable plastic cup with the

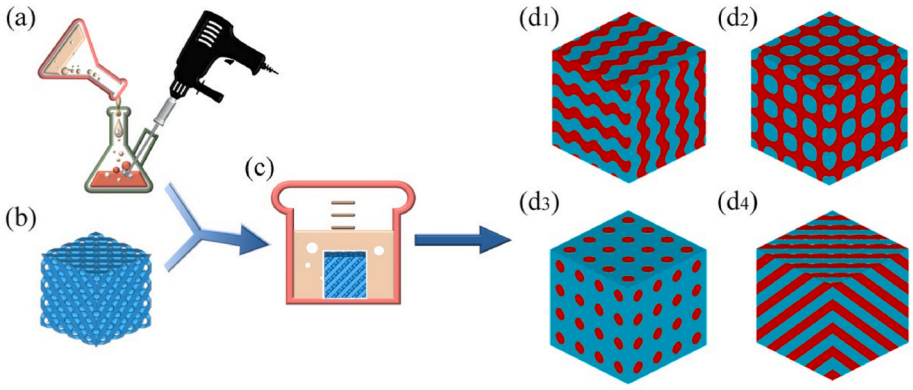

Fig. 3. Fabrication of polyurethane reinforced triply periodic minimal composite structure; (a) The electric variable-speed stirrer ANgni stirs mixture; (b) Original triply periodic minimal structure; (c) Bottom-up automatic foaming process; (d_1) Film Gyroid; (d_2) Film IWP; (d_3) Film Primitive; (d_4) Film Diamond, where the blue part is foam and the red part is Nylon.

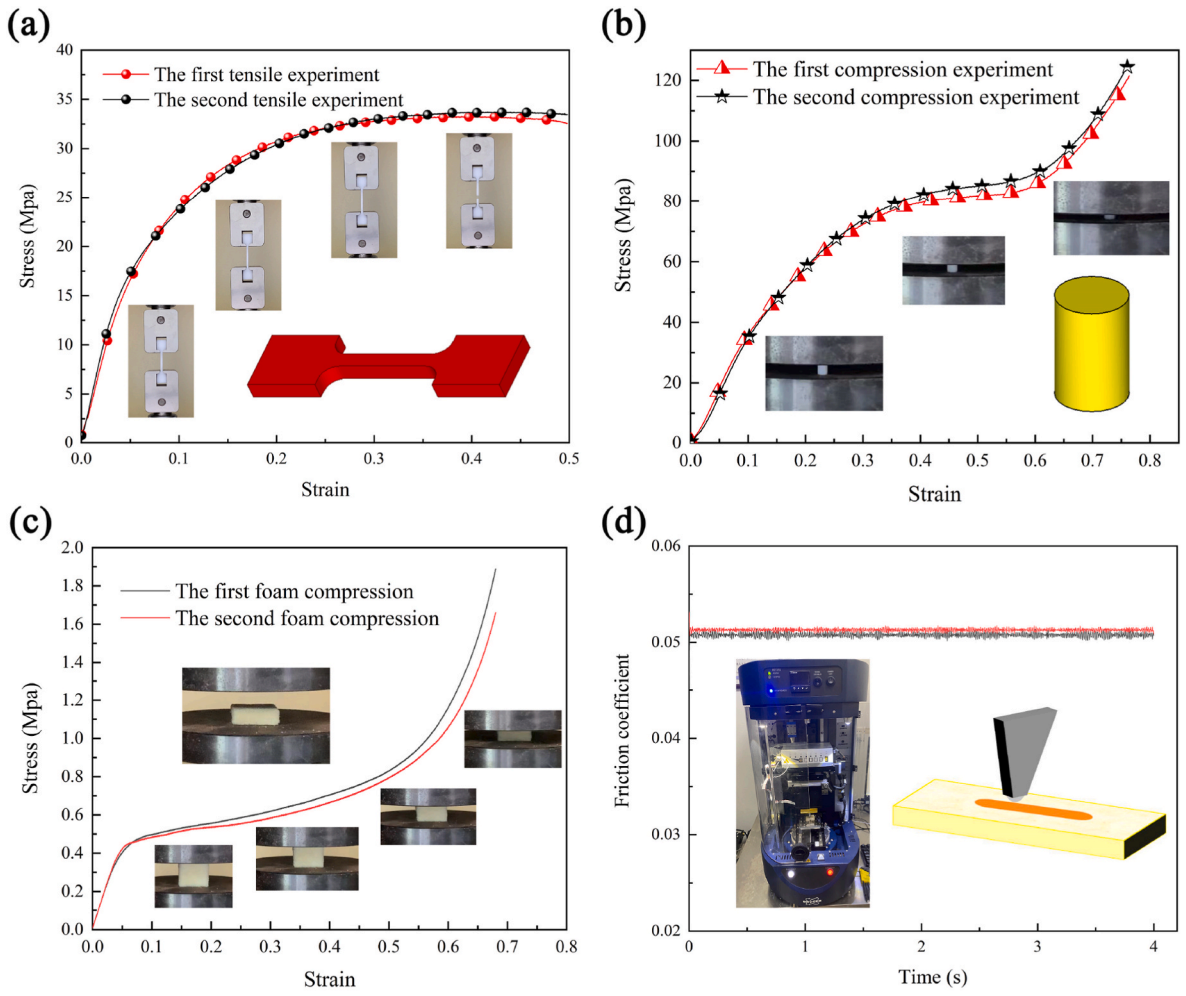

Fig. 4. Material properties measuring results; (a) Nylon tensile measuring results; (b) Nylon compression measuring results; (c) Polyurethane foam compression measuring results; (d) Friction coefficient measuring result between materials. The detailed size of Materials' testing samples is found in attachment 3.

triply periodic minimal structure. During the foaming process, the foam slowly fills the triply periodic minimal structure from bottom to top, as shown in Fig. 3. Remove the polyurethane-enhanced triply periodic minimal composite structure from the disposable plastic cup. Manual cutting is performed according to the triply periodic minimal structure size. They are placed at room temperature for 2 h. Finally, filled triply periodic minimal composite structures corresponding to triply periodic minimal structures are obtained: Film Gyroid, Film IWP, Film Primitive, and Film Diamond, as shown in Fig. 3.

2.2. Structural additive manufacturing and material

Four nylon triply periodic minimal samples are manufactured with FS300 SLS Machine. The Selective Laser Sintering (SLS), which uses Nylon powder to layer-up and form 3D solid parts, has a smaller heat affected zone compared to other additive manufacturing methods. It is

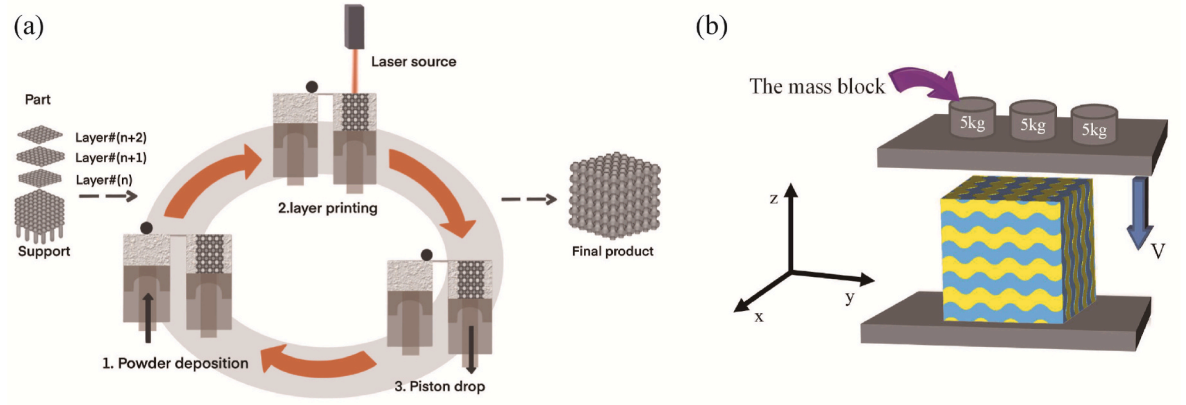

Fig. 5. The process of structural tests. (a) The process of additive manufacturing; (b) Structural compression and impact process.

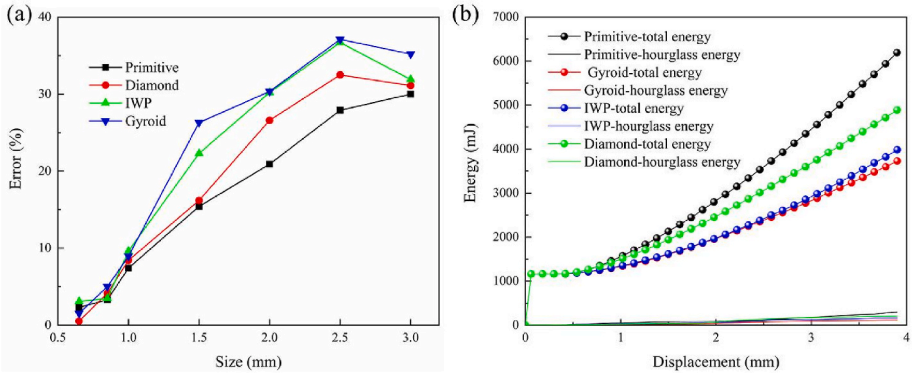

Fig. 6. The mesh independence of structures; (a) The calculation error under different mesh sizes; (b) Compressed hourglass energy and total energy at 0.85 mm mesh size.

capable of producing complex, high-accuracy parts. To utilize SLS, the required CAD model, including the geometry shape and support of the part, needs to be imported first. Then, the model is sliced into layers with a predefined thickness T, and processing parameters are set up, such as laser power, scanning speed, and scanning pitch. After that, a layer of powder is pre-spread with a roller, and the laser beam selectively melts the powder layer according to the geometric information of the sliced CAD model. Following solidification, the powder shelf rises to allow for the deposition of the next layer, and the process is repeated until the designed shape is completed, as shown in Fig. 5(a). The SLS scanning speed is 7.62 mm/s. The SLS laser power is 22 w. The preheating temperature of the construction cabin is 413 k, and the printing temperature of the construction cabin is 442 k. To protect the Nylon powder from oxidation, the manufacturing process takes place in an argon atmosphere and the 3D-printed model is shown in Fig. 2.

The material properties of the samples are tested by Instron 5963 Machine. The extension speed of the machine punch is set to 1 mm/min. In the compression measuring, the load is applied until the Nylon specimens are flattened. In the tensile measuring, the tensile load is applied until the Nylon samples are broken. In the numerical calculation, the engineering stress and strain are transformed into nominal stress and strain for simulation in Eq. (5) and Eq. (6).

$$\sigma_{\text{nom}} = \sigma_{\text{engineering}}\left(1 + \varepsilon_{\text{engineering}}\right) \tag{5}$$

$$\varepsilon_{\text{nom}} = \ln\left(1 + \varepsilon_{\text{engineering}}\right) \tag{6}$$

Note that when drawing Fig. 4, the force-displacement data recorded during the test are converted into engineering stress and strain by taking the cross-sectional area of the testing architecture and the initial height. Specific material testing results of engineering stress and strain are shown in Fig. 4(a)–(c).

Using the friction testing machine (BRUKER), friction coefficient tests are conducted on two types of materials as shown in Fig. 4(d). The spherical slider of the testing machine is replaced with the 3D-printed nylon ball with a diameter of 6 mm, and the polyurethane material sample is fixed on the lower platform. A predetermined pressure load of 4 N is applied for the friction coefficient test between the two materials. According to the test results, the friction coefficient between the two material samples is 0.051, as shown in Fig. 4(d). Polyurethane foam has excellent waterproofing [53]. The drainage method using a 100 ml measuring cylinder is used to test the average density of polyurethane foam, to improve the accuracy of the numerical analysis. Because the polyurethane foam can float up, the steel block is used to drop the polyurethane foam to prevent floating and improve the testing accuracy in the experiment of polyurethane foam by drainage method. The formula of polyurethane foam density is

$$\rho_{foam} = \frac{M_{foam}}{V_{foam}} = \frac{M_{foam}}{V_{all} - V_{water} - V_{steel\ block}} \tag{7}$$

where V_{foam} is the volume for polyurethane foam; V_{all} is the volume after adding polyurethane foam and steel blocks; V_{water} is the volume of water; $V_{steel\ block}$ is the volume of the steel block; M_{foam} is the mass of polyurethane foam. The density of polyurethane foam is 80 kg/m^3.

2.3. Structural model

The nonlinear dynamic finite element program LS-DYNA is used to simulate the compressive response of the triply periodic minimal structure. The tetrahedral solid element in LS-DYNA is used to mesh partition for the triply periodic minimal structure. Bio-inspired structures and the rigid wall are set to #Surface to Surface Contact for avoiding mutual penetration between components in the process of deformation. The constitutive material is #MAT_Elastic-Plastic Material. The density of Nylon is 1100 kg/m^3, and the elastic modulus is 1000 MPa. Poisson's ratio is 0.38. The yield stress is 21 MPa [47,48]. The ideal elastic-plastic constitutive model is used to characterize the true stress-strain relationship of Nylon. Polyurethane foam is simulated by #MAT_CRUSHABLE _ FOAM. The parameters that need to be input are as follows: density, elastic modulus, poisson ratio, stress-strain curve and damping coefficient 0.15 for controlling strain rate sensitivity. Because the foam is soft, it is easy to generate errors such as negative volume. Therefore, the stress-strain curve can be adjusted appropriately to make it denser and harder in the dense stage.

In the compression simulation of the triply periodic minimal structure, the triply periodic minimal specimen is fixed on the rigid plate. The bottom of the rigid support plate is fully constrained, and the quasi-static compression in the Z direction is performed by another moving rigid plate with a constant speed, as shown in Fig. 5. However, because the simulation calculation is too expensive compared to the quasi-static experimental speed (1 mm/min), the loading speed of the moving rigid plate v = 0.01 m/s is given in this study to ensure the accuracy and efficiency of the compression simulation. The surface-to-surface contact algorithm and self-contact algorithm are defined to simulate the contact behavior between different components after compression deformation [7,15]. The friction coefficient in the kinematics simulation is 0.051, as shown in Fig. 4(d).

To address the contact damage between dissimilar materials in the polyurethane-enhanced triply periodic minimal composite structure, the mesh boundary of the conjoin part is bonded by common nodes. The element deletion method is used for the triply periodic minimal structure model, and the failure criterion is employed according to Nylon attributes. Hourglass control is adopted for implicit surface structure compression simulation to avoid zero energy deformation modes. The total energy and hourglass energy are compared to ensure the accuracy

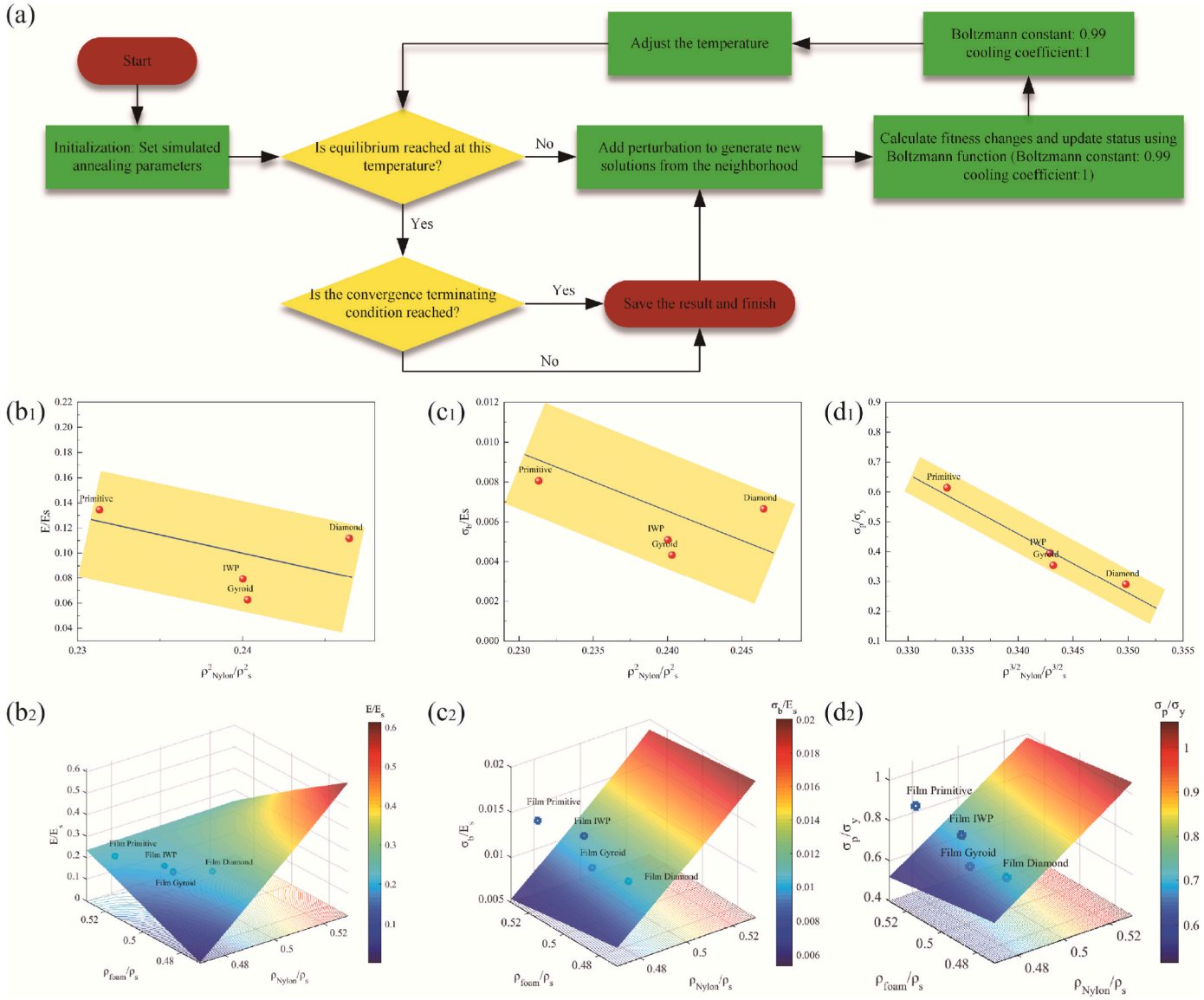

Fig. 7. Theoretical prediction results. (a) Schematic diagram of simulated annealing algorithm; (b_1) The relation between relative elastic modulus E/E_S and relative density ρ^2/ρ_S^2 of triply periodic minimal structures with a single material; (b_2) The relation between relative elastic modulus E/E_S and relative density ρ/ρ_S of polyurethane-enhanced triply periodic minimal composite structures; (c_1) The relation between relative elastic modulus σ_b/E_S and relative density ρ^2/ρ_S^2 of triply periodic minimal structures with a single material; (c_2) The relation between relative elastic modulus σ_b/E_S and relative density ρ/ρ_S of polyurethane-enhanced triply periodic minimal composite structures; (d_1) The relation between relative elastic modulus σ_p/σ_y and relative density ρ^2/ρ_S^2 of triply periodic minimal structures with a single material; (d_2) The relation between relative elastic modulus σ_p/σ_y and relative density ρ/ρ_S of polyurethane-enhanced triply periodic minimal composite structures.

of numerical analysis, as shown in Fig. 6(b).

3. Mesh independence analysis

The mesh-independent validation of 0.65 mm, 0.85 mm, 1 mm, 1.5 mm, 2 mm, 2.5 mm and 3 mm are used to find the most efficient and accurate mesh size. Since the numerical calculating results are equivalent to the structural deformation of the given shape function, the stiffness of the numerical analysis can be larger than the ideal solution. The finer the numerical mesh, the closer the solution. Then, when comparing the mesh independence, the mesh size (0.5 mm) is taken as the energy reference E_0 for the mesh-independence analysis. The error formula of mesh independence analysis is

$$a_{\text{Error}} = \frac{E - E_0}{E_0} \times 100\% \tag{8}$$

where E is the energy absorption with different mesh sizes. a_{Error} is the error.

When bio-inspired units are compressed by 4 mm, the absorbed energy error of bio-inspired units is shown in Fig. 6. The energy absorption error tends to be stable and the energy absorption error is less than 5% when the mesh size is less than 0.85 mm. It can be determined from Fig. 6 that the size of the simulation elements is 0.85 mm. And the hourglass energy is less than 5% of the total compression energy, which shows that the numerical analysis is effective.

4. Structural theoretical analysis

In quasi-static compression, the energy of the elastic system is stable because quasi-static compression behavior refers to the structural deformation response under a slow and continuous rate of compressive

load. In this case, the structural deformation rate is very slow (usually much less than the deformation rate under yield strength response), and the changes in inertia and momentum can be ignored. Therefore, it can be regarded as equivalent to a static (i.e. no motion) deformation situation. When the structure is subjected to elastic deformation under load, it is in the conservation of external work and internal energy, which is equivalent to the first principle of thermodynamics. The implicit surface structure is subjected to a force of size F, which is a conservative force. Each instantaneous displacement of the load compression is x, and the work of the load on this displacement is equivalent to the force potential energy, that is, the work is independent of the path. W is

$$W = Fx \tag{9}$$

where, W is the virtual work at this time.

In quasi-static compression, the total potential energy of the structure is constant, which means that the first variation of the total potential energy is 0, namely

$$\delta\Pi = 0 \tag{10}$$

where, Π is the total potential energy of the structure.

Therefore, the first-order variation of the work done by the external force can be equivalent to the first-order variation of the structural strain energy and U is the structural strain energy.

$$\delta U + \delta W = 0 \tag{11}$$

After the quasi-static compression exceeds the elastic stage, the structure undergoes plastic deformation, and the strain energy can dissipate with the structural deformation, that is, the plastic hinge energy dissipation E.

$$\delta E + \delta U + \delta W = 0 \tag{12}$$

The triply periodic minimal structure and polyurethane-enhanced triply periodic minimal composite structures show elastic deformation at the initial stage of compression. Under minimum strain rate, Euler theory can be used to calculate the elastic deformation of the structure with the relative density $\frac{\rho}{\rho_S}$ greater than 0.1 [51]. According to Euler theory [51], the structural micro-deformation is

$$\Delta L = \frac{\int\left(\int FL\mathrm{d}l\right)\mathrm{d}l}{E_S I} \tag{13}$$

$$I = \int_s y^2 \mathrm{d}s \tag{14}$$

where, E_S is the elastic modulus of Nylon material. y is the distance between the cross section at a certain position of the structure and y axis. s is the cross-sectional area at different locations at a certain height of the structure. l is the distance from the reference point to the load F.

The structural elastic modulus is [51].

$$E = \frac{\sigma}{\varepsilon} = \frac{E_S I}{S_L L^2} \tag{15}$$

where,

$$\sigma = \frac{F}{S_L} = \frac{\Delta L E_S I}{S_L \int\left(\int L\mathrm{d}l\right)\mathrm{d}l} \tag{16}$$

$$\varepsilon = \frac{\Delta L}{L} \tag{17}$$

S_L is the cross-sectional area of the contact position.

The structural relative density is

$$\frac{\rho}{\rho_S} = \frac{M_{\mathrm{Actual}}/V}{M_{\mathrm{Nylon}}/V_S} = \frac{M_{\mathrm{Actual}} V_S}{M_{\mathrm{Nylon}} V} \tag{18}$$

where, $V_S \propto \int_l \int_S \mathrm{d}S\mathrm{d}l$, $V = L^3$. ρ is the structural density. ρ_S is the Nylon material density. L is the overall height of the structure. S is the cross-sectional area at different locations at different heights of the structure.

$$\frac{\rho}{\rho_S} \propto \frac{\int_S \mathrm{d}S}{L^2} \tag{19}$$

According to Eq. (15), obtain

$$\frac{E}{E_S} \propto \left(\frac{\rho}{\rho_S}\right)^2 \tag{20}$$

That is

$$\frac{E}{E_S} = A_1\left(\frac{\rho}{\rho_S}\right)^2 + B_1 \tag{21}$$

where, A_1 and B_1 are the constants.

The relations between relative elastic modulus and relative density for triply periodic minimal structures with a single material in this paper are shown in Fig. 7(b_1).

For the rigid-flexible coupling composite structure,

$$\frac{E}{E_S} = A_2\left(\frac{\rho}{\rho_S}\right)^2_{\mathrm{Nylon}} + B_2\left(\frac{\rho}{\rho_S}\right)^2_{\mathrm{foam}} + C_2\left(\frac{\rho_{\mathrm{Nylon}}\rho_{\mathrm{foam}}}{\rho_{S-\mathrm{Nylon}}\rho_{S-\mathrm{foam}}}\right)^2_{\mathrm{Coupling}} + D_2 \tag{22}$$

where, A_2, B_2, C_2 and D_2 are the constants. $\left(\frac{\rho_{\mathrm{Nylon}}\rho_{\mathrm{foam}}}{\rho_{S-\mathrm{Nylon}}\rho_{S-\mathrm{foam}}}\right)^2_{\mathrm{Coupling}}$ is the coupling parts between different materials.

The relations between relative elastic modulus and relative density for polyurethane-enhanced triply periodic minimal composite structures are obtained using the simulated annealing algorithm, as shown in Fig. 7 (b_2).

The buckle force of the structure at the initial stage of compression is

$$F = \frac{n^2 \pi E_s I}{L^2} \tag{23}$$

where, $I = \int_s y^2 \mathrm{d}s$. $n = 0.7$ [23].

So buckle stress is

$$\sigma_{\mathrm{b}} \propto \frac{E_S I}{L^4} \tag{24}$$

$$\frac{\sigma_{\mathrm{b}}}{E_{\mathrm{S}}} \propto \frac{\int_s y^2 \mathrm{d}s}{L^4} \propto \left(\frac{\rho}{\rho_{\mathrm{S}}}\right)^2 \tag{25}$$

That is

$$\frac{\sigma_{\mathrm{b}}}{E_{\mathrm{S}}} = A_3\left(\frac{\rho}{\rho_{\mathrm{S}}}\right)^2 + B_3 \tag{26}$$

where, A_3 and B_3 are the constants.

For the rigid-flexible coupling composite structure,

$$\frac{\sigma_{\mathrm{b}}}{E_{\mathrm{S}}} = A_4\left(\frac{\rho}{\rho_S}\right)^2_{\mathrm{Nylon}} + B_4\left(\frac{\rho}{\rho_S}\right)^2_{\mathrm{foam}} + C_4\left(\frac{\rho_{\mathrm{Nylon}}\rho_{\mathrm{foam}}}{\rho_{S-\mathrm{Nylon}}\rho_{S-\mathrm{foam}}}\right)^2_{\mathrm{Coupling}} + D_4 \tag{27}$$

where, A_4, B_4, C_4 and D_4 are the constants.

The relationship between structural buckle stress and material elastic modulus is shown in Fig. 7(c_1). The relations between structural buckle stress and material elastic modulus for polyurethane-enhanced triply periodic minimal composite structures are shown in Fig. 7(c_2).

When plastic failure occurs in bio-inspired structures, the moment at the failure position of bio-inspired structures is

$$M_{\mathrm{p}} = \sigma_{\mathrm{y}} I t \tag{28}$$

where, σ_y is the Nylon yield stress of the bio-inspired structure. t is the centrifugal distance inside the section.

The force is perpendicular to the bio-inspired structure, so the bending moment of the bio-inspired structure can be expressed as *FL*. Obtain

$$\sigma_p \propto \frac{M_p}{L^3} \tag{29}$$

Combine Eq. (25) with Eq. (28), get

$$\frac{\sigma_p}{\sigma_y} \propto \left(\frac{\rho}{\rho_s}\right)^{\frac{3}{2}} \tag{30}$$

That is

$$\frac{\sigma_p}{\sigma_y} = A_5\left(\frac{\rho}{\rho_s}\right)^{\frac{3}{2}} + B_5 \tag{31}$$

where, A_5 and B_5 are the constants.

For the rigid-flexible coupling composite structure,

$$\frac{\sigma_p}{\sigma_y} = A_6\left(\frac{\rho}{\rho_S}\right)^{\frac{3}{2}}_{\text{Nylon}} + B_6\left(\frac{\rho}{\rho_S}\right)^{\frac{3}{2}}_{\text{foam}} + C_6\left(\frac{\rho_{\text{Nylon}}\rho_{\text{foam}}}{\rho_{S-\text{Nylon}}\rho_{S-\text{foam}}}\right)^{\frac{3}{2}}_{\text{Coupling}} + D_6 \tag{32}$$

where, A_6, B_6, C_6 and D_6 are the constants.

The relationship between structural plastic stress and material yield stress is shown in Fig. 7(d_1). The relations between structural plastic stress and material yield stress for polyurethane-enhanced triply periodic minimal composite structures are shown in Fig. 7(d_2).

When a concentrated mass block M with a speed of V_0 impacts the structure, the structure is deeply affected by the shock wave. The structure in front of the shock wave is stationary, while the structure behind it has the strain of ε_0 and the relative density of ρ_S. The relative density of the structure in the area behind the shock wave becomes $\rho_S/(1-\varepsilon_D)$, and the speed of this part is deformed at the same speed as the concentrated mass block. The stress of the structure behind the shock wave suddenly increases to σ_D, with a velocity of V_D, and the height of the compacted structure is L, with a corresponding uncompressed height of $L_0 = L/(1-\varepsilon_D)$. The plastic work required for the structure to reach a strain of ε_D is $\sigma_P\varepsilon_D AL/(1-\varepsilon_D)$, where A is the cross-sectional area of the structure. This follows the principle of conservation of energy.

$$\frac{1}{2}\left(M + \frac{\rho_S}{1-\varepsilon_D}AL\right)V_D^2 + \sigma_P\varepsilon_D A\frac{L}{1-\varepsilon_D} = \frac{1}{2}MV_0^2 \tag{33}$$

The plastic wave speed of the structure is

$$C_P = \sqrt{\frac{(\sigma_D - \sigma_P)}{\varepsilon_D\rho_S}} \tag{34}$$

So the particle velocity is

$$V_D = C_P\varepsilon_D \tag{35}$$

When there exists a time increment δT, the momentum of the structure at the shock wave front is

$$(\sigma_D - \sigma_P)A\cdot\delta T = \frac{\rho_S AC_P\cdot\delta T\cdot V_D}{1-\varepsilon_D} \tag{36}$$

So

$$\sigma_D = \sigma_P + \frac{\rho_S C_P V_D}{1-\varepsilon_D} \tag{37}$$

Combine Eq. (33) and Eq. (37), get

$$\sigma_D = \sigma_P + \frac{\rho_S}{\varepsilon_D}\frac{MV_0^2 - 2\sigma_P AL\cdot\varepsilon_D/(1-\varepsilon_D)}{M + \rho_S AL/(1-\varepsilon_D)} \tag{38}$$

As the length L of the compressed structure increases, the structural load decreases. When $L_0 = 0$, initial maximum stress at the moment of impact is

Table 2
The constants of the relation between relative elastic modulus and relative density.

Constant	A_1		B_1	
Original structures	−2.07		0.59	
Constant	A_2	B_2	C_2	D_2
Polyurethane-enhanced composite structures	46.92	40.62	−166.3	−11.22
Constant	A_3		B_3	
Original structures	−0.121		0.035	
Constant	A_4	B_4	C_4	D_4
Polyurethane-enhanced composite structures	0.194	−0.051	0.11	−0.03
Constant	A_5		B_5	
Original structures	−20.55		7.45	
Constant	A_6	B_6	C_6	D_6
Polyurethane-enhanced composite structures	7.31	−1.212	1.279	−11.16

$$\sigma_D = \sigma_P + \frac{\rho_S V_0^2}{\varepsilon_D} \tag{39}$$

Overall, the impact load consists of quasi-static stress and dynamic enhancement caused by inertia effect. Under the action of impact load on the structure, the anti-shock performance of different stages of structural deformation is positively correlated with the static compressive performance of the structure, that is, $\sigma_D \propto \left(\frac{\rho}{\rho_S}\right)^2$.

The constants of relations are shown in Table 2.

5. Performance analysis of the triply periodic minimal composite structure

5.1. Evaluation indicators

To compare the mechanic characteristics more accurately and efficiently, this paper adopts evaluation indicators (internal energy absorption *EA*, specific energy absorption *SEA*, specific energy absorption about volume *SEAV* impact acceleration *a*)

EA is the standard to measure the deformation resistance of the structure itself. Structural energy absorption under the compression is calculated, as shown in Eq. (40)

$$EA = \int_0^{x_0} F\mathrm{d}x \tag{40}$$

where, x_0 is the magnitude of structural deformation. F is the load against deformation.

SEA is the most essential standard to measure the defensive ability of the structure and also balances an important criterion for material utilization efficiency, as shown in Eq. (41)

$$SEA = \frac{EA}{M} \tag{41}$$

where, M is the structural mass.

SEAV is an important essential criterion to measure the configurational capability of the structure, as shown in Eq. (42)

$$SEAV = \frac{EA}{V} \tag{42}$$

where, V is the structural volume.

a is the contact impact acceleration of the structure under high-speed impact. In the process of body protection, the smaller the impact load is, the more beneficial it is to be used as a protective structure. When the impact mass is the same, the impact acceleration can be used as a measure of the impact load. The smaller the impact acceleration after the impact, the more impact energy is absorbed by the structure during

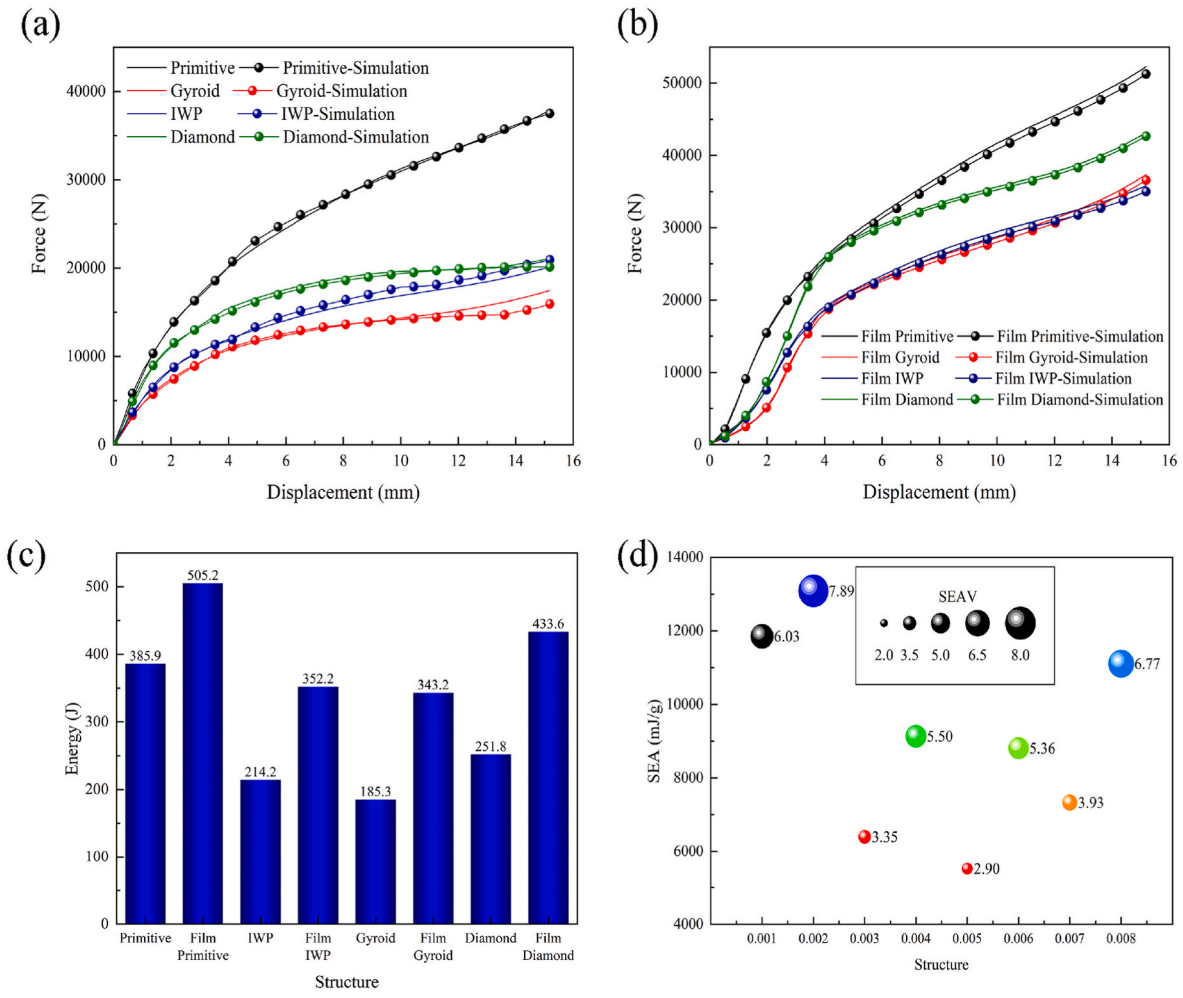

Fig. 8. The compressive characteristics of triply periodic minimal structures and polyurethane-enhanced triply periodic minimal composite structures; (a) The compressive load behavior of four triply periodic minimal structures; (b) The compressive load behavior of polyurethane-enhanced triply periodic minimal composite structures; (c) The structural compression energy absorption comparison; (d) The structural compression SEA and SEAV comparison.

the impact process, resulting in a significant decrease in the impact load.

5.2. Quasi-static compression characteristics of triply periodic minimal composite structures

The sample is placed on the platform of the WDT Series_KQL system, and at the same time, the cross-sectional normal direction of the structural specimen is parallel to the loading direction, as shown in Fig. 5(b). The accuracy and sensitivity of the displacement and force sensors are calibrated, and the control of the loading rate is ensured to be less than 20 N/min. After the start of loading, the instrument controller of the universal testing machine applies a compressive load at a rate of 1 mm/min. During the quasi-static compression process, the force-displacement sensor is used to monitor the deformation and force changes of the structure, and real-time output of the structural compression force-displacement curve, as shown in Fig. 8(a) and (b). For each model, three samples are tested. Fig. 8(a) and (b) shows the compressive load behavior of triply periodic minimal structures and polyurethane-enhanced triply periodic minimal composite structures, respectively. The numerical analysis considers the manufacturing defects and test errors that may cause changes in the experimental results from the setting of Nylon material properties. The calculation results are consistent with the experimental results.

As the compression displacement increases, the deformation finiteness of the triply periodic minimal structures gradually becomes

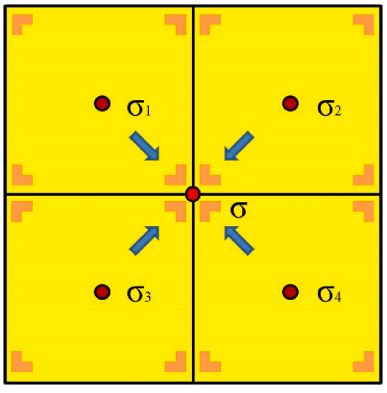

Fig. 9. The averaged stress method.

nonlinear (the stress gradually reaches the material yield), as shown in Fig. 8. This process is initiated by local deformation/stress concentration in some 'weak' position. These stress concentration sites are circled in Fig. 9, where they first undergo bending loading. Therefore, the loading flat region in Fig. 8 is the result of material yielding due to the stress concentration of one or more locations in triply periodic minimal structures. The initial load of the four triply periodic minimal structures is linear, and the relationship between the overall mean load of triply

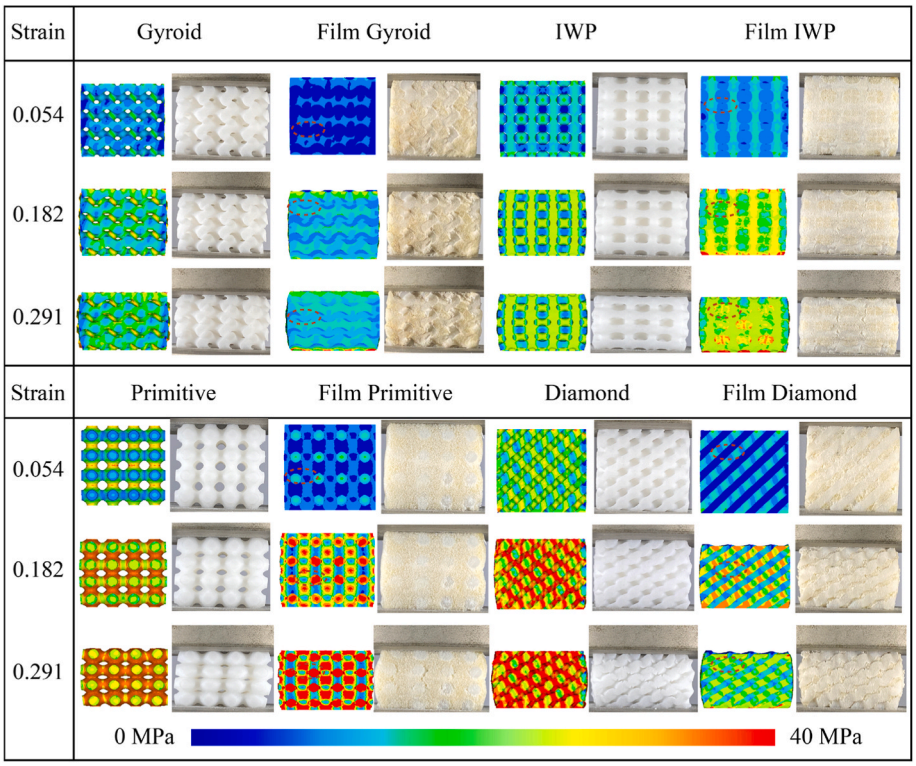

Fig. 10. The structural deformation modes and stress distribution.

periodic minimal structures is $F_P > F_D > F_I > F_G$. However, the load of the polyurethane-enhanced triply periodic minimal composite structure increases slowly with the increase of extrusion displacement. Then, the structural load changes linearly and the compression load becomes gentle. The relationship between the overall average load of the four polyurethane-enhanced triply periodic minimal composite structures is $F_P > F_D > F_I > F_G$. The average load of polyurethane-enhanced triply periodic minimal composite structures is also greater than that of the corresponding triply periodic minimal structures, which is increased by more than 30%. The energy absorption of the polyurethane-enhanced composite structure is improved compared to the triply periodic minimal structure, and EA is increased by more than 30%. Furthermore, based on Eq. (41) and Eq. (42), SEA and SEAV of both the biomimetic structures and the polyurethane-enhanced composite structures are calculated. The results show that the polyurethane-enhanced composite structures are effective in improving the mechanical properties of structures, with SEA increased by over 10% and SEAV increased by over 30%.

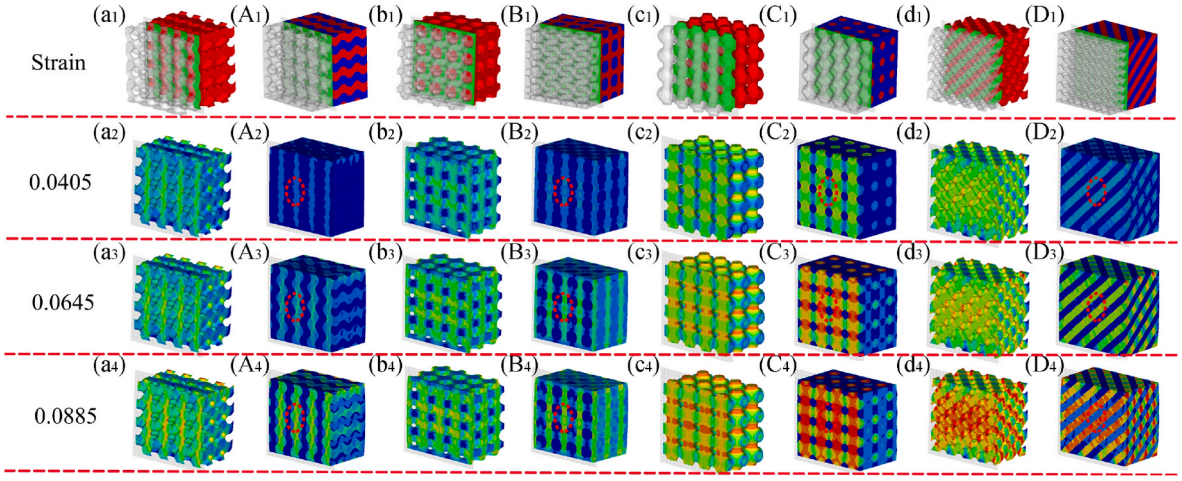

Fig. 11. Changes of structural stress distribution with compression strain of 0.0405, 0.0645, and 0.0885. (a_1) Gyroid cross section; ($a_{2\text{-}4}$) Stress distribution of Gyroid cross section with compression strain of 0.0405, 0.0645, and 0.0885; (A_1) Film Gyroid cross section; ($A_{2\text{-}4}$) Stress distribution of Film Gyroid cross section with compression strain of 0.0405, 0.0645, and 0.0885; (b_1) IWP cross section; ($b_{2\text{-}4}$) Stress distribution of IWP cross section with compression strain of 0.0405, 0.0645, and 0.0885; (B_1) Film IWP cross section; ($B_{2\text{-}4}$) Stress distribution of Film IWP cross section with compression strain of 0.0405, 0.0645, and 0.0885; (c_1) Primitive cross section; ($c_{2\text{-}4}$) Stress distribution of Primitive cross section with compression strain of 0.0405, 0.0645, and 0.0885; (C_1) Film Primitive cross section; ($C_{2\text{-}4}$) Stress distribution of Film Primitive cross section with compression strain of 0.0405, 0.0645, and 0.0885; (d_1) Diamond cross section; ($d_{2\text{-}4}$) Stress distribution of Diamond cross section with compression strain of 0.0405, 0.0645, and 0.0885; (D_1) Film Diamond cross section; ($D_{2\text{-}4}$) Stress distribution of Film Diamond cross section with compression strain of 0.0405, 0.0645, and 0.0885.

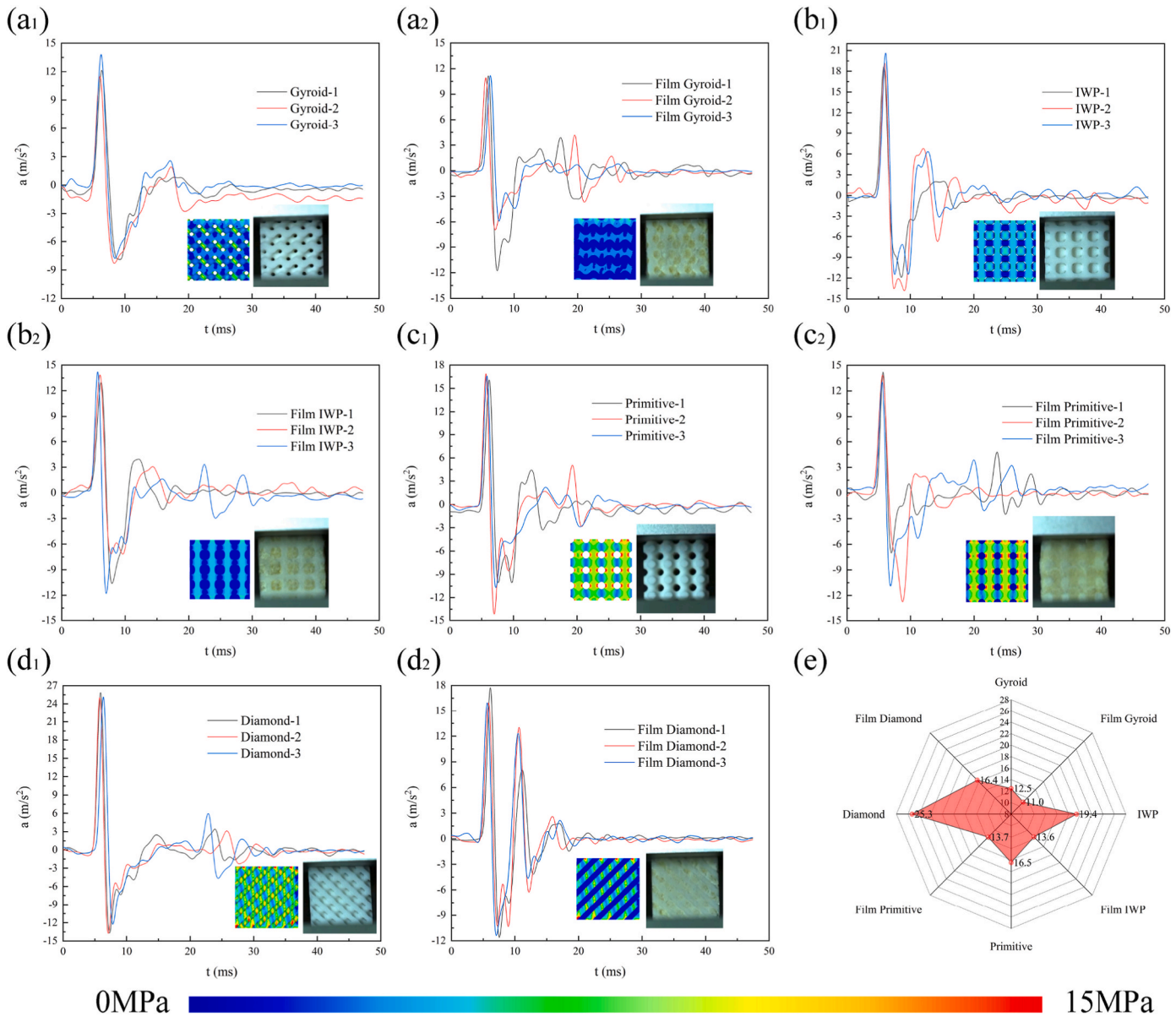

Fig. 12. Impact acceleration data; (a_1) The experimental impact acceleration of Gyroid; (a_2) The experimental impact acceleration of Film Gyroid; (b_1) The experimental impact acceleration of IWP; (b_2) The experimental impact acceleration of Film IWP; (c_1) The experimental impact acceleration of Primitive; (c_2) The experimental impact acceleration of Film Primitive; (d_1) The experimental impact acceleration of Diamond; (d_2) The experimental impact acceleration of Film Diamond; (e) The maximum impact acceleration comparison. The structural deformation modes are the impact response under the maximum acceleration and detailed videos of structural impact modes captured by high-speed photography FASTCAM Nova R2 can be found in attachment 2.

As shown in Fig. 9. The averaged method is used to display the stress distribution cloud map of the structures, where the load on each element node is the average value of the centroid values of each element surrounding the node, $\sigma = \frac{\sigma_1+\sigma_2+\sigma_3+\sigma_4}{4}$.

Fig. 10 includes the structural deformation modes and stress distribution under different strains. The force-displacement relationship of all structures is linear in the strain range of 0–30%. Due to the lack of instability such as buckling or large bending deformation of the structures in this paper, the stress is almost instantaneously distributed in all parts of the structures, and the response of all structures to the compressive load is uniform. The results of the finite element analysis are compared with the corresponding experimental observations. A detailed frame-by-frame comparison of the video recorded by the compression experiments and the numerical structural deformation provides additional evidence of the models' abilities to capture the deformation resistance of the micro-lattice structure, as shown in Fig. 10. When the compression starts, the elastic response of the whole structure is localized, and the stress is mainly concentrated on the vertical configuration of the component. Because the vertical part of these structures is in the direction of load support, it is mainly supported by bending resistance. Due to the load dispersion effect of foam, the load distribution of the polyurethane-enhanced composite structure is not only in the vertical direction but also in the transverse direction at the initial stage of deformation, as shown in Fig. 11.

To better observe the dispersion effect of the foam on the overall bearing capacity of the triply periodic minimal structure, composite structures are subjected to structural shear to see the internal deformation and structural stress distribution. The shear interface is shown in the green surface in Fig. 11. The red circle in Fig. 11 indicates that the increase of local strain leads to the vertical deformation of the structure, where the strain increases locally. At about 4% strain, the stress is in the yield region, and the middle of the structure is affected by local strain

increase.

The soft-hard alternating-filled structure is equivalent to the rigid-flexible coupling mixture. The compression results strongly prove that the foam-filled design has better impact resistance than the single-material design. The extrusion expansion of the foam leads to a more energy dissipation path. The stress deforms simultaneously through the hard and soft components during the coupling interface. It results in the deviation of the load transfer direction and furthers the impact energy dissipation. Due to this expansion through the foam, the energy transfer path is allowed to deviate in the foam. All these factors (more energy dissipation and transfer path deviation) work together to improve the crashworthiness of polyurethane-enhanced triply periodic minimal composite structures. This bio-inspired composite design of rigid-flexible coupling filling structure is crucial to the new design paradigm of the next generation of rapid prototyping on demand.

5.3. Crashworthiness analysis of triply periodic minimal composite structures

To investigate the effect of foam filling on the structural crashworthiness, an impact block with a mass of 20 kg is used to impact all specimens in the free fall of 50 cm high, and the experimental impact acceleration is compared, as shown in Fig. 12. The specific impact is photographed by high-speed photography FASTCAM Nova R2, as shown in attachment 2.

With the progress of the free-falling impact, it shows that the impact load of four polyurethane-enhanced composite samples is more stable than the original structures. This is the result that the local foam deformation absorbs the deformation energy of the Nylon material. Therefore, adding foam to the design of a protective structure can improve the structural protection characteristics. Compared with the response of pure hard Nylon specimens, the addition of foam increases the energy transfer path inside the structure when the whole structure is impacted, so the crashworthiness is improved. The reduction of normalized Mises stress is proved in the design of the polyurethane-enhanced structure, and the reduction of the impact acceleration of the polyurethane-enhanced triply periodic minimal composite structure is more than 13.6%. The impact energy is more widely spread due to the rigid-flexible energy dissipation effect of the polyurethane-enhanced composite structure design. Structural foam filling is a reasonable way to dissipate the impact energy of the protective structure.

6. Conclusion

Inspired by the micro-curved structure and microfiber filling of the feather, four triply periodic minimal structures and four polyurethane-enhanced triply periodic minimal composite structures are designed. The compressive properties and crashworthiness of triply periodic minimal structure and polyurethane-enhanced triply periodic minimal composite structure are studied. The structural load distribution and deformation modes are investigated, and the following conclusions are:

(1) The prediction model based on Euler theory and simulated annealing algorithm can well predict the mechanical relationships of composite structures at the compression and impact stage.
(2) The expansion of the foam allows the compression energy transfer path to deviate in the foam, and the load distribution is not only in the vertical direction but also in the transverse direction. Polyurethane-enhanced composite structures are effective in improving the mechanical properties of structures, with F increased by over 30%, SEA increased by over 10% and SEAV increased by over 30%.
(3) All these factors (more energy dissipation and transfer path deviation) work together to improve the crashworthiness of polyurethane-enhanced triply periodic minimal composite structures. The reduction of the impact acceleration of polyurethane-enhanced triply periodic minimal composite structure is more than 13.6%.

This bio-inspired composite design of rigid-flexible coupling filling structure is crucial to the new design paradigm of the next generation of rapid prototyping on demand.

Author statement

Ruiyao Liu: Writing–original draft, Writing–review and editing, Visualization, Project administration, Data curation, Formal analysis, Methodology, Software, Formal analysis, Guofeng Yao: Writing–review and editing, Visualization, Supervision, Conceptualization, Validation, Luming Sha: Writing–review and editing, Zhenglei Yu: Writing–review and editing, Visualization, Funding acquisition, Resources, Conceptualization, Validation, Ping Liang: Writing–review and Funding acquisition, Software, Validation, Chunyang Han: Writing–review and editing, Keyi Zhu: Writing–review and editing, Lei Dong: Writing–review and editing, Zezhou Xu: Writing–review, Jundong Zhang: Writing–review, Yunting Guo: Writing–review and Revision.

Declaration of competing interest

The authors declare that they have no known competing financial interests or personal relationships that could have appeared to influence the work reported in this paper

Data availability

Data will be made available on request.

Acknowledgements

This work is supported by National Key R&D program of China (2022YFE0138500), National Natural Science Foundation of China (No. 51975246), Science and Technology Development Program of Jilin Province, China (20230203031SF), National Natural Science Foundation of Chongqing (CSTB2022NSCQ-MSX0225), Capital construction funds within the budget of Jilin Provincial Development and Reform Commission (2023C041-4), The 5th Batch of Special Grants from China Postdoctoral Science Foundation (before the station) (2023TQ0129).

Appendix A. Supplementary data

Supplementary data to this article can be found online at https://doi.org/10.1016/j.compscitech.2023.110197.

References

[1] K.P. Dharmasena, D.T. Queheillalt, H. Wadley, P. Dudt, Y. Chen, D. Knight, A. Evans, V. Deshpande, Dynamic compression of metallic sandwich structures during planar impulsive loading in water, Eur. J. Mech. 29 (1) (2010) 56–67.
[2] S. Daynes, S. Feih, W.F. Lu, J. Wei, Optimisation of functionally graded lattice structures using isostatic lines, Mater. Des. 127 (8) (2017) 215–223.
[3] L. Yang, R. Mertens, M. Ferrucci, C. Yan, Y. Shi, S. Yang, Continuous graded Gyroid cellular structures fabricated by selective laser melting: design, manufacturing and mechanical properties, Mater. Des. 162 (2019) 394–404.
[4] L. Cheng, J. Bai, A.C. To, Functionally graded lattice structure topology optimization for the design of additive manufactured components with stress constraints-ScienceDirect, Comput. Methods Appl. Mech. Eng. 344 (2019) 334–359.
[5] M. Dalia, E. Mohamed, Lattice structures and functionally graded materials applications in additive manufacturing of orthopedic implants: a review, J. Manuf. Mater. Process. 1 (2) (2017) 13.
[6] Y. Wang, L. Zhang, S. Daynes, H. Zhang, S. Feih, M.Y. Wang, Design of graded lattice structure with optimized mesostructures for additive manufacturing, Mater. Des. 142 (2018) 114–123.
[7] C. Liu, Z. Du, W. Zhang, Y. Zhu, X. Guo, Additive manufacturing-oriented design of graded lattice structures through explicit topology optimization, J. Appl. Mech. (2017) 84.

[8] J. Zhang, Z. Wang, L. Zhao, Dynamic response of functionally graded cellular materials based on the Voronoi model, Compos. B Eng. 85 (2016) 176–187.
[9] J.G. Seob, M.J. Buehler, Multiscale mechanics of triply periodic minimal surfaces of three-dimensional graphene foams, Nano Lett. 18 (2018) 4845–4853.
[10] T. Tancogne-Dejean, D. Mohr, Stiffness and specific energy absorption of additively-manufactured metallic BCC metamaterials composed of tapered beams, Int. J. Mech. Sci. 141 (2018) 101–116.
[11] Z. Zheng, Y. Liu, J. Yu, S.R. Reid, Dynamic crushing of cellular materials: continuum-based wave models for the transitional and shock modes, Int. J. Impact Eng. 42 (2012) 66–79.
[12] W. Song, Compressive properties and collapse behavior of additively-manufactured layered-hybrid lattice structures under static and dynamic loadings, Thin-Walled Struct. 157 (2020), 107153.
[13] A. Alhammadi, O. Al-Ketan, K.A. Khan, M. Ali, R. Rowshan, R.K. Abu Al-Rub, Microstructural characterization and thermomechanical behavior of additively manufactured AlSi10Mg sheet cellular materials, Mater. Sci. Eng. 791 (2020), 139714.
[14] H. Yin, X. Zheng, G. Wen, C. Zhang, Z. Wu, Design optimization of a novel bio-inspired 3D porous structure for crashworthiness, Compos. Struct. 255 (2021), 112897.
[15] L. Xiao, W. Song, Additively-manufactured functionally graded Ti-6Al-4V lattice structures with high strength under static and dynamic loading: experiments, Int. J. Impact Eng. 111 (2017) 255–272.
[16] J. Zhang, S. Zhang, W.C. Cui, X.L. Zhao, W.X. Tang, F. Wang, Buckling of circumferentially corrugated cylindrical shells under uniform external pressure, Ships Offshore Struct. 14 (8) (2019).
[17] M. Oba, Y. Inaba, N. Kobayashi, H. Ike, T. Tezuka, T. Saito, Effect of femoral canal shape on mechanical stress distribution and adaptive bone remodelling around a cementless tapered-wedge stem, Bone Joint Res. 5 (9) (2016) 362–369.
[18] T.J. Feo, D.J. Field, R.O. Prum, Barb geometry of asymmetrical feathers reveals a transitional morphology in the evolution of avian flight, Proc. Biol. Sci. 282 (2015), 20142864.
[19] B. Liu, W. Cao, L. Zhang, K.Y. Jiang, P. Lu, A design method of Voronoi porous structures with graded relative elasticity distribution for functionally gradient porous materials, Int. J. Mech. Mater. Des. 17 (2021) 1–21.
[20] Y. Jin, H.Y. Kong, X.Y. Zhou, G.Y. Li, J.K. Du, Design and characterization of sheet-based gyroid porous structures with bioinspired functional gradients, J. Mater. 13 (17) (2020) 3844.
[21] L. Yuan, S. Ding, C. Wen, Additive manufacturing technology for porous metal implant applications and triple minimal surface structures: a review, Bioact. Mater. 4 (1) (2019) 56–70.
[22] S.A.M. Tofail, E.P. Koumoulos, A. Bandyopadhyay, S. Bose, L. O'Donoghue, C. Charitidis, Additive manufacturing: scientific and technological challenges, market uptake and opportunities, Mater. Today 21 (1) (2018) 22–37.
[23] A.A. Zadpoor, Additively manufactured porous metallic biomaterials, J. Mater. Chem. B 7 (6) (2019) 4088–4117.
[24] L. Yang, C. Yan, C. Han, P. Chen, S. Yang, Y. Shi, Mechanical response of a triply periodic minimal surface cellular structures manufactured by selective laser melting, Int. J. Mech. Sci. 148 (2018) 149–157.
[25] A. Yanez, A. Cuadrado, O. Martel, H. Afonso, D. Monopoli, Gyroid porous titanium structures: a versatile solution to be used as scaffolds in bone defect reconstruction, Int. J. Mech. Sci. 140 (2018) 21–29.
[26] Z. Li, L. Shen, K. Wei, Z. Wang, Compressive behaviors of fractal-like honeycombs with different array configurations under low velocity impact loading, Thin-Walled Struct. 163 (2021), 107759.
[27] Z. Wang, X. Wang, T. Gao, C. Shi, Mechanical behavior and deformation mechanism of triply periodic minimal surface sheet under compressive loading, Mech. Adv. Mater. Struct. 28 (19) (2020) 2057–2069.
[28] Z. Chen, X. Wu, Y.M. Xie, Z. Wang, S. Zhou, Re-entrant auxetic lattices with enhanced stiffness: a numerical study, Int. J. Mech. Sci. 178 (2020), 105619.
[29] C. Bonatti, D. Mohr, Mechanical performance of additively-manufactured anisotropic and isotropic smooth shell-lattice materials: simulations & experiments, J. Mech. Phys. Solid. 122 (2018) 1–26.
[30] Z. Chen, Y.M. Xie, X. Wu, Z. Wang, Q. Li, S. Zhou, On hybrid cellular materials based on triply periodic minimal surfaces with extreme mechanical properties, Mater. Des. 183 (2019), 108109.
[31] M. Shen, W. Qin, B. Xing, W. Zhao, S. Gao, Y. Sun, T. Jiao, Z. Zhao, Mechanical properties of 3D printed ceramic cellular materials with triply periodic minimal surface architectures, J. Eur. Ceram. Soc. 41 (2) (2020) 1481–1489.
[32] O. Al-Ketan, R. Rowshan, R.A. Al-Rub, Topology-mechanical property relationship of 3D printed strut, skeletal, and sheet based periodic metallic cellular materials, Addit. Manuf. 19 (2018) 167–183.
[33] H. Yin, Z. Liu, J. Dai, G. Wen, C. Zhang, Crushing behavior and optimization of sheet-based 3D periodic cellular structures, Compos. B Eng. 182 (2019), 107565.
[34] P. Tran, C. Peng, Triply periodic minimal surfaces sandwich structures subjected to shock impact, J. Sandw. Struct. Mater. 23 (6) (2020), 109963622090555.
[35] Y. Kao, A.R. Amin, N. Payne, J. Wang, B.L. Tai, Low-velocity impact response of 3D-printed lattice structure with foam reinforcement, Compos. Struct. 192 (2018) 93–100.
[36] B.J. Ramirez, U. Misra, V. Gupta, Viscoelastic foam-filled lattice for high energy absorption, Mech. Mater. 127 (2018) 39–47.
[37] G. Hou, Z. Yu, D. Ye, The influence of laser power and scanning speed on the dimensional accuracy of SLS formed parts, IOP Conf. Ser. Earth Environ. Sci. 791 (1) (2021), 012154.
[38] H. Zhu, G. Hou, Optimization of SLS forming parameters in the dimensional accuracy of formed parts, E3S Web Conf. 233 (11) (2021), 01069.
[39] A.I. Idriss, J. Li, Y.L. Guo, Y.W. Wang, X.D. Li, Z.Q. Zhang, E.A. Elfaki, Sintering quality and parameters optimization of sisal fiber/PES composite fabricated by selective laser sintering (SLS), J. Thermoplast. Compos. Mater. (2020) 1–15.
[40] D. Catana, M. Pop, D. Brus, Comparison between tests and simulations regarding bending resistance of 3D printed PLA structures, Polymers 13 (24) (2021).
[41] B. Caroline, F.L. Stan, G. Giovanna, A.H. Martien, D.A. Patrick, Numerical analysis of the crystallization kinetics in SLS, Addit. Manuf. 33 (2020), 101126.
[42] D.I. Brus, Comparison between the test and simulation results for PLA structures 3D printed, bending stressed, Molecules 26 (11) (2021) 3325.
[43] A.K. Mishra, H. Chavan, A. Kumar, Effect of material variation on the uniaxial compression behavior of FDM manufactured polymeric TPMS lattice materials, Mater. Today: Proc. 46 (17) (2021) 7752–7759.
[44] K. Monkova, M. Vasina, M. Zaludek, P.P. Monka, J. Tkac, Mechanical vibration damping and compression properties of a lattice structure, Materials 14 (6) (2021) 1502.
[45] R. Gautam, S. Idapalapati, S. Feih, Printing and characterisation of Kagome lattice structures by fused deposition modelling, Mater. Des. 137 (2018) 266–275.
[46] M.A. Rifaie, A. Mian, R. Srinivasan, Compression behavior of three-dimensional printed polymer lattice structures, Proc. Inst. Mech. Eng. 233 (8) (2019) 1574–1584.
[47] X. Xu, Y. Zhang, J. Fang, X. Chen, Z. Liu, Y. Xu, Y. Gao, Axial mechanical properties and robust optimization of foam-filled hierarchical structures, Compos. Struct. 289 (2022), 115501.
[48] K. Wang, Y. Liu, J. Wang, J. Xiang, S. Yao, Y. Peng, On crashworthiness behaviors of 3D printed multi-cell filled thin-walled structures, Eng. Struct. 254 (2022), 113907.
[49] T.N. Sullivan, A. Pissarenko, S.A. Herrera, D. Kisailus, V.A. Lubarda, M.A. Meyers, A lightweight, biological structure with tailored stiffness: the feather vane, Acta Biomater. 41 (2016) 27–39.
[50] T.N. Sullivan, B. Wang, H.D. Espinosa, M.A. Meyers, Extreme lightweight structures: avian feathers and bones, Mater. Today 20 (2017) 377–391.
[51] L.J. Gibson, M.F. Ashby, Cellular Solids: Structure and Properties, Pergamon Press, 1997.
[52] S. Rajagopalan, R.A. Robb, Schwarz meets Schwann: design and fabrication of biomorphic and durataxic tissue engineering scaffolds, Med. Image Anal. 10 (5) (2006) 693–712.
[53] H.D. Liu, Z.Y. Liu, M.B. Yang, Q. He, Superhydrophobic polyurethane foam modified by graphene oxide, J. Appl. Polym. Sci. 130 (5) (2013).